Fracture behavior of solid electrolyte LATP material based on micro-pillar splitting method

Gang Yan[1*], Jürgen Malzbender[1], Shuo Fu[1], Jürgen Peter Gross[1], Shicheng Yu[2], Rüdiger-A. Eichel[2,3,4], Ruth Schwaiger[1,5]

[1] Forschungszentrum Jülich GmbH, Institute of Energy and Climate Research (IEK), Microstructure and Properties of Materials (IEK-2), 52425 Jülich, Germany

[2] Forschungszentrum Jülich GmbH, Institute of Energy and Climate Research (IEK), Fundamental Electrochemistry (IEK-9), 52425 Jülich, Germany

[3] Forschungszentrum Jülich GmbH, Helmholtz-Institute Münster: Ionics in Energy Storage (IEK-12), 48149 Münster, Germany

[4] RWTH Aachen, Institute of Physical Chemistry, 52074 Aachen, Germany

[5] RWTH Aachen University, Chair of Energy Engineering Materials, 52056 Aachen, Germany

Abstract

The NASICON type solid electrolyte LATP is a promising candidate for all-solid-state Li-ion batteries considering energy density and safety aspects. To ensure the performance and reliability of batteries, crack initiation and propagation within the electrolyte need to be suppressed, which requires knowledge of the fracture characteristics. In the current work, micro-pillar splitting was applied to determine the fracture toughness of LATP material for different grain orientations. The results are compared with data obtained using a conventional Vickers indentation fracture (VIF) approach. The fracture toughness obtained via micro-pillar splitting test is 0.89 ± 0.13 MPa·m$^{1/2}$, which is comparable to the VIF result, and grain orientation has no significant effect on the intrinsic fracture toughness. Being a brittle ceramic material, the effect of pre-existing defects on the toughness needs to be considered.

Keywords: Solid state battery, Solid electrolyte, LATP, fracture toughness, anisotropy, micro-pillar splitting test

[*] g.yan@fz-juelich.de; tel: +492461616477; fax: +492461613699

Introduction

All-solid-state lithium batteries currently obtain increasing attention in the energy storage field due to their high energy capacity and improved safety aspects compared to the conventional lithium batteries containing liquid electrolytes [1, 2]. The key component of the all-solid-state lithium batteries is the solid electrolyte, for which a series of different solid electrolyte materials have been developed recently [3]. The sodium zirconium phosphate (NASICON) type electrolyte, $Li_{1+x}Al_xTi_{2-x}(PO_4)_3$ (LATP) ceramic material is one of the most promising potential inorganic electrolytes that is known to exhibit the electrochemical and chemical stability upon contact with lithium metal as well as high ionic conductivity [4-6].

The electrolyte of the battery suffers from the cyclic chemical expansion due to the lithium ions intercalation and extrapolation in the electrodes as well as the thermal expansion during charging/discharging, which requires mechanical stability of the electrolytes materials to ensure long-term operation [7-11]. In addition, the formation of lithium dendrites and their propagation leading to micro-cracks inside the electrolytes have been reported as a challenge for the battery life [7-10]. Hence, the mechanical properties of the solid electrolyte materials, such as elastic modulus (E), hardness (H), and fracture toughness (K_{IC}), need to be investigated. In particular, the fracture toughness of the electrolyte appears to be quite critical as it indicates the materials' resistance to crack propagation, which might occur during battery operation leading to eventual component failure.

The fracture behavior of solid electrolytes has been assessed in a number of publications using different methods. The effect of micro-cracking on ionic conductivity in LATP has been reported by Jackman et al. [12], indicating twice the ionic conductivity of fine-grained LATP compared to coarse-grained LATP due to reduced fracture at grain boundaries; the fracture toughness of LATP material evaluated via single-edge pre-cracked beam method was 1.1 ± 0.3 $MPa{\cdot}m^{1/2}$. As reported by Athanasiou et al. [13], the LATP material can be toughened through the addition of

reduced graphene oxide (rGO), resulting in fracture toughness values of 1.1 MPa·$m^{1/2}$, 2.4 MPa·$m^{1/2}$ and 3.7 MPa·$m^{1/2}$ for spark plasma sintered LATP, 1% rGO LATP and 5% rGO LATP, respectively. Both single-edge notched beam and Vickers indentation methods were used in that study. Dashjav et al. [14] investigated the mechanical stability of LATP material with 1.5% SiO_2 reporting the Weibull modulus and characteristic fracture strength via ball-on-3-ball test as 13 and 168 MPa, respectively, with 90% confidence intervals of 8-17 and 161-175 MPa, respectively.

Fracture testing in the case of, for example, single-edge notched beams typically requires a large number of pre-cracked test specimens of a certain size, which often limits the applicability of such conventional standard methods due to materials availability [15]. Therefore, for thin functional ceramics that are often produced nowadays, three types of methods are used to evaluate the fracture toughness, i.e. pre-cracked beam tests (e.g., single-edge notched bend test, middle-crack test, double torsion testing), Vickers indentation fracture (VIF) test, and micro-pillar or micro-cantilever tests [16].

The VIF test adopts a standard Vickers indenter to induce an impression on a polished intact specimen surface creating a plastically deformed zone underneath the imprint as well as cracks running outward and radially downward from the imprint [17]. To obtain a good estimate of the fracture toughness via VIF testing, a critical factor is to precisely determine the crack length. The micro-pillar splitting method is based on the indentation of micro-pillars [18, 19]. The crack nucleates inside the pillar once a critical load is achieved. Knowing the original pillar dimensions, the fracture toughness can then be evaluated. The micro-pillar splitting method has been developed only recently and still needs to be developed and improved further, in particular for smaller samples [15, 19].

LATP possesses a rhombohedral phase structure indicating anisotropic mechanical properties, which has indeed been verified experimentally for both elastic modulus and

hardness by indentation mapping [20]. The results indicate that the rotation angle from basal plane to prismatic plane can significantly affect the mechanical properties. The experimental elastic modulus and hardness of LATP were reported to be in the range of 107 to 150 GPa and 5.5 to 10.0 GPa, respectively [20], which is similar to the elastic moduli of 81 and 115 GPa and hardness of 7.1 ± 0.4 GPa reported in [12]. The anisotropy of the elastic modulus was also confirmed by first principle calculations [21] yielding a range of 139.0 to 152.5 GPa for the elastic modulus of the $LiTi_2(PO_4)_3$ type material.

Recent studies applied the micro-pillar splitting method and the conventional VIF method [22, 23] to evaluate the fracture toughness of Al-doped $Li_7La_3Zr_2O_{12}$ (LLZO) electrolyte. The fracture toughness values of LLZO obtained by micro-pillar splitting was ~ 1 $MPa \cdot m^{1/2}$ and comparable to VIF results [22]. The grain boundaries appeared to enhance the fracture toughness slightly as verified by testing single grains and grain agglomerates [23]. Mughal et al. [24] investigated the fracture toughness of the cathode material $Li_xMn_2O_4$ under different charging states using high-speed nanoindentation, which facilitates a robust and efficient evaluation of elastic modulus and hardness, indicating that the fracture toughness can be affected by volume change, defect density and stress associated with lithium diffusion. The micro-pillar splitting test, therefore, enables a local characterization of the fracture behavior of battery materials facilitating advanced studies of the failure behavior. In this work, we studied the fracture toughness of solid electrolyte material LATP by micro-pillar splitting for different grain orientations.

Experimental

The preparation of the LATP material was conducted following the procedure specified in [25, 26]. Firstly, the raw powders for LATP were synthesized via a conventional sol-gel method. A mixture of $Ti(OC_3H_8)_4$ and NH_4OH (Aldrich, 30% solution) in a ratio of 1:2 was used to obtain the gelatinous precipitates, which was then stored in 100 ml of deionized water. A clear solution of $H_2[TiO(C_2O_4)_2]$ was produced

with addition of 200 ml of 1 M oxalic acid (Aldrich, 99.9%), then mixed with stoichiometric $Al(NO_3)_3 \cdot 9H_2O$ (Aldrich, 99.9%), $(NH_4)_2HPO_4$ (Aldrich, 98%) and 5% excess $LiCOOCH_3 \cdot 2H_2O$ (Aldrich, 98%). The mixed solution was stirred and heated to 80 °C with a hot plate to gain well mixed precipitates. Pre-annealing of the precipitates was conducted at 850 °C for 5 h in air, thereafter the obtained powders were milled and introduced into a cylinder mold for uniaxial pressing at 40 kN. The compressed cylindrical pellets were subsequently isostatically pressed with 1425 kN load for 10 s and synthesized for 11 h at 1100 °C to obtain LATP samples. The relative density estimated based on Archimedes' principle with water was 96.7% [20]. The total ionic conductivity of the LATP determined by electrochemical impedance spectroscopy was 0.18 mS/cm [20], which is in good agreement with the value of 0.2 mS/cm reported in [12, 27] and higher than that reported for some other typical solid electrolytes, such as LIPON (3.3×10^{-6} S/cm) [28] or LISICON (~ 10^{-6} S/cm) [29-31].

The microstructures of the LATP samples were characterized by scanning electron microscopy (SEM, SUPRA 50VP, Zeiss Microscopy, Oberkochen, Germany). The software "AnalySIS pro" was used with line intercept technique for further analysis yielding a grain size of 12.1 ± 5.9 μm of the sample. X-ray diffraction (XRD, Bruker 4 Endeavour spectrometer rigged with a LYNXEY 1D detector and a DIFFRAC^{plus} BASIC package 2009, Bruker AXS GmbH, Karlsruhe, Germany) was adopted to characterize the LATP crystal structure and phases. The XRD theta-2 theta scans were conducted at room temperature with Cu-K_α radiation in the range of 10° to 100° with scanning step of 0.02° / 2 s. Being a solid electrolyte material, the electrochemical property of the LATP is essential for its practical usage. Thus, the conductivity of the LATP pellets was assessed via a potentiostat equipped with a frequency response analyzer (Bio-Logic, SP-300, Seyssinet-Pariset, France) at frequencies from 7 MHz to 1 Hz and voltage amplitude of 10 mV at 25 °C using a climate chamber (Binder KB 115, Tuttlingen, Germany). The pellet with thickness of 0.3 mm and diameter of 11.3 mm was gauged, of which surface was polished to remove potential contaminations as well as to obtain a flat surface, and a thin gold coating was sputtered on both sides of

the pellet [26]. The basic properties of the LATP sample are summarized in Table 1.

Table 1. Properties of the studied LATP material

Sample	Structure	Grain size (μm)	Relative density	Conductivity (S/cm)
LATP	Rhombohedral (R-3c h)	12.1 ± 5.9	96.72%	1.83×10^{-4}

One LATP specimen was embedded into water-free resin and polished with a series of abrasive compounds (smallest grain size of 0.2 μm) together with polyethylene glycol (PEG) achieving a smooth sample surface. PEG polishing was employed to protect the sample from reaction with water, which can lead to a composition and microstructure change at the surface [32]. The grain orientations of the LATP sample were determined using electron backscatter diffraction (EBSD, with NordLys detector, Oxford Instruments, High Wycombe, UK).

The open source MATLAB toolbox MTEX [33] was used to analyze the crystallographic texture on the basis of the EBSD data. The LATP material possesses a rhombohedral phase structure, which can be computed into a hexagonal lattice like the corundum mineral [34]. Based on the Euler angles, the angle between the surface plane to the basal plane and to the prismatic plane can be calculated. The details of the procedure can be found in [20]. As reported in [20], only the angle Ω from the basal (0001) plane to the vertical prismatic plane affects the mechanical properties, i.e., the elastic modulus and hardness, of LATP material. Considering the symmetric character of the hexagonal crystal system, the angle Ω is converted in the range of $[0, \pi/2]$ and used for the pillar splitting test results analysis.

The micro-pillars were fabricated by focused ion beam (FIB) milling (Auriga, Zeiss Microscopy GmbH, Oberkochen, Germany) at an acceleration voltage of 30 kV and moderate beam currents of 2-15 nA. The pillars were positioned in selected grains and milled to diameter and height of 10 μm maintaining a fixed aspect ratio (height /

diameter) of 1 to eliminate any potential residual stress effect on the top surface of the pillars [18, 19]. In total two batches of 8 pillars each were fabricated in differently oriented grains.

The fracture toughness of LATP was determined from the micro-pillar splitting approach utilizing a Berkovich tip [18, 19] and compared to the results obtained from the conventional VIF method [15]. The micro-pillar splitting test was carried out using a Nanotest Xtreme nanoindenter (Micromaterials Ltd., Wrexham, England) equipped with an optical microscope. Before the indentation, the pillar surfaces were scanned with the indenter tip at an imaging load of 0.002 mN and step length of 0.2 µm to ensure that the indentation was positioned exactly in the center of the pillar. The indentation experiments were conducted at a load rate of 2.5 mN/s until a maximum load of 50 mN was reached. From the load-displacement curves the critical loads for crack nucleation appearing as distinct kinks in the curves can be extracted. The fracture toughness of the pillars was then calculated applying the following equation [19]:

$$K_c = \gamma \cdot \frac{P_c}{R^{3/2}} \tag{1}$$

where P_c is the critical load leading to pillar splitting, R the radius of the pillar and γ a dimensionless coefficient considering the crack propagation, indenter geometry, as well as the material properties. The coefficient γ has been identified evaluating a number of brittle materials having different modulus-to-hardness-ratios E/H [18, 19], yielding:

$$\gamma = 0.0149 \cdot \left(\frac{E}{H}\right) + 0.057 \tag{2}$$

Equation 2 was further expanded and validated by Cohesive-Zone Finite Element Modeling for materials with E/H ratio ranging from 5 to 31 and Poisson's ratios of 0.20 - 0.30 [35-37]. Elastic modulus and hardness of this LATP material were reported as 107 - 150 GPa and 5.5 - 10.0 GPa, respectively [20].

The macroscopic fracture toughness was estimated by the conventional VIF method, for which the elastic modulus and hardness of the LATP were determined in advance using nanoindentation. The indentation tests were carried out using a Fischer instrument with a Vickers tip (Fischerscope H100 Microtester, Helmut Fischer GmbH, Sindelfingen, Germany) to different loads of 50, 100, 300 and 500 mN to evaluate the effect of the porosity. For each load 20 indentations were conducted, with loading and unloading times of 10 s, holding period of 1 s and acquisition rate of 10 Hz. The indentations were conducted in the center of the large grains. The E and H were determined from the load-displacement data based on the Oliver-Pharr methodology [38] assuming an elastic modulus E_i = 1141 GPa and Poisson's ratio ν_i = 0.07 of the diamond tip and Poisson's ratio of ν_s = 0.25 for the LATP material [12, 21].

For the VIF test, a series of loads of 0.5 N, 1 N and 3 N and holding time of 15 s were applied to induce the crack. At each load 5 indentations were employed and the produced imprints were measured immediately after the VIF experiment in the SEM to prevent any effect relating to moisture and carbon dioxide in the air. Commonly, radial-median or Palmqvist indentation crack modes appear for ceramic materials [39]. When the ratio (l/a) of the measured crack length l to the half diagonal a is in the range of [0.25, 2.5], as verified in the current study, a Palmqvist crack relationship can be used, which is given in detail in [40].

Results and discussion

The sample was carefully inspected after surface preparation by SEM. As shown in Fig. 1(a), the pores were homogeneously distributed in the LATP sample. Pores were found in both the grain boundaries and the grain interiors as shown in Fig. 1(b). At the grain boundaries, the pores have a rather irregular shape, whereas in the interior they appear more or less spherical due to the hydrostatic pressure of residual air, which was conserved during grain growth in the pre-annealing process [41]. The grain boundaries of the LATP sample are clearly visible, which is beneficial for the pillar fabrication and

also conducting the low load indentation test in large grains.

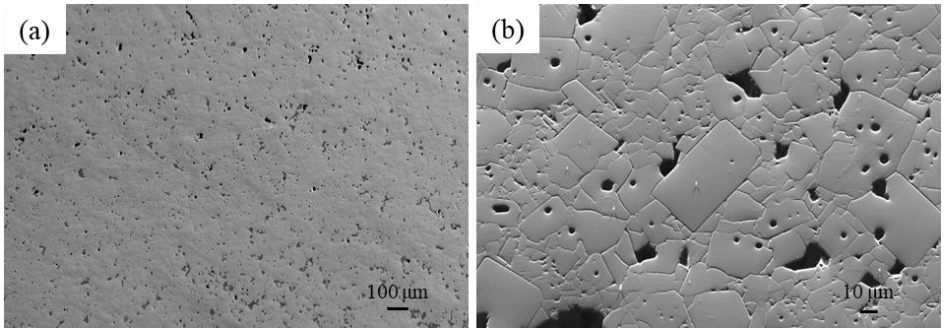

Figure 1. SEM micrographs of polished LATP sample at different magnifications: a) sample surface exhibiting a homogeneous distribution of pores, b) pores were found in the grain interior as well as at the grain boundaries, which are clearly visible.

The polished as-sintered LATP samples were characterized by XRD to analyze the phase structure. The XRD results indicated that the sample was mainly composed of LATP in rhombohedral structure with a minor amount of secondary phase of $AlPO_4$. The presence of a secondary phase can be attributed to the Li evaporation from LATP during high temperature sintering, during which the Al dopant level exceeded the solubility enabling the formation of the precipitates [42]. As demonstrated in previous work [20], the secondary phase is mainly present at the grain boundaries in small amounts and, within the scope of this study, its effect on the mechanical properties can be neglected.

SEM micrographs of the micro-pillars together with the corresponding EBSD maps are shown in Fig. 2. Based on the high quality of the EBSD maps, it can be concluded that defects and residual stresses in the surface layer had been removed during the polishing process. Therefore, any effects of residual stresses on the fracture toughness determined by micro-pillar splitting can be ruled out. As shown in Fig. 2(c) and (d), the grains of the LATP specimen were randomly oriented. The big grains, which did not appear to have pores, were selected in order to reduce the influence of the pores on the pillar splitting.

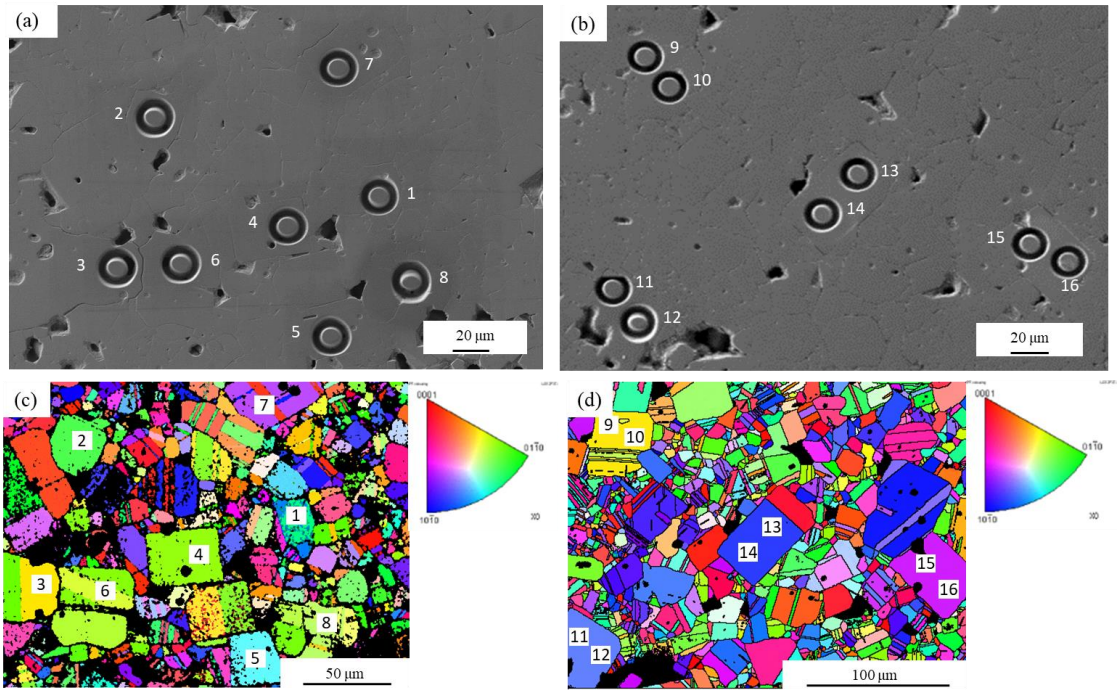

Figure 2. (a), (b) SEM micrographs of micro-pillars prepared by FIB positioned in selected locations of the LATP. (c), (d) EBSD maps showing the orientation of the selected grains.

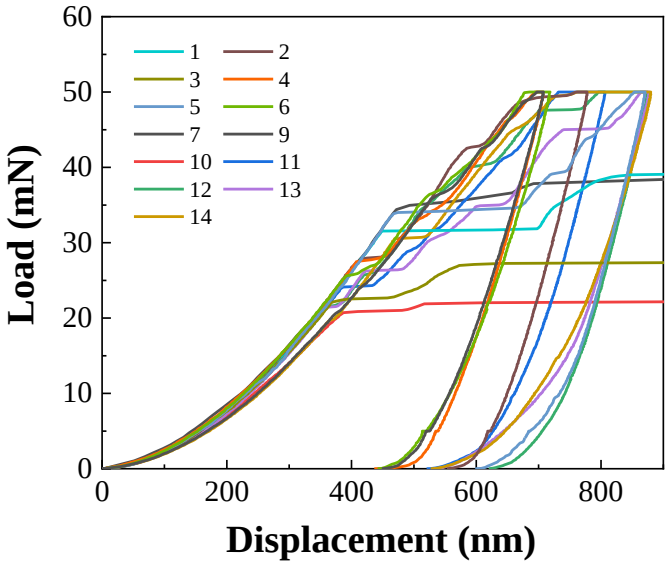

Figure 3. Load-displacement curves of indents into FIB-milled LATP micro-pillars. The critical loads (at the first pop-in) were in the range from 21.7 to 35.9 mN.

The load-displacement curves obtained by the micro-pillar splitting tests are shown

in Fig. 3. In total the data of 13 pillars were used to calculate the fracture toughness, since pillars 8, 15 and 16 were crushed at low loads (see Fig. 6), likely caused by the presence of pores underneath the surface, see also [43]. Clear pop-ins can be seen in Fig. 3 and the critical loads are in the range of 21.7 to 35.9 mN. For some curves additional pop-ins appeared after the critical load had been surpassed indicating that additional cracks or crushing had occurred.

Based on the results presented in [20], the values of E and H as a function of the rotation angle between the crystal plane to the basal plane are shown in Fig. 4(a). The corresponding E to H ratios are shown in Fig. 4(b). Noting that the easy-slip model [44, 45] cannot predict the absolute value of the hardness, but rather a relative hardness, the hardness of 5.5 GPa at the prismatic plane was used as a reference value for normalization based on the experimental results in [20]. For the following fracture toughness calculation, we used the predicted elastic modulus and hardness of 111 - 166 GPa and 5.5 - 10.0 GPa, respectively, as intrinsic properties of LATP [20]. The ratio of E to H has a minimum of around 15 at the basal plane and increases to an almost constant level of around 20 as shown in Fig. 4(b).

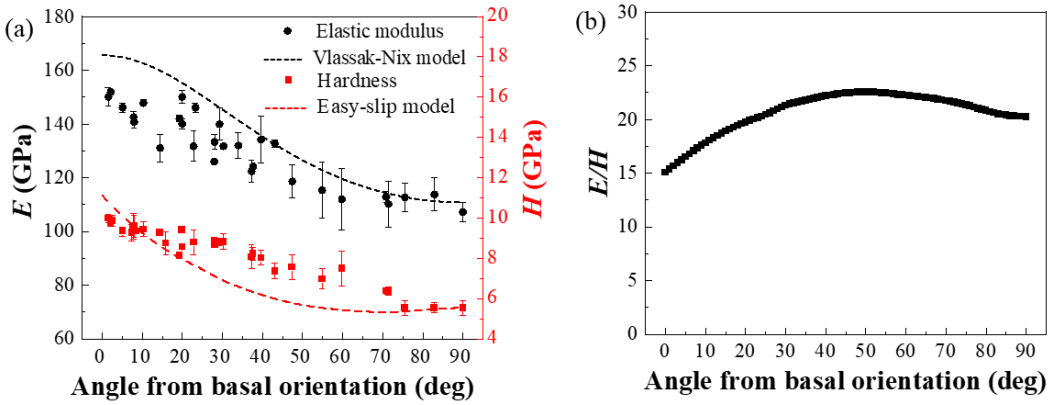

Figure 4. (a) The elastic modulus and hardness of LATP material as a function of rotation angle from the basal plane to the prismatic plane, and (b) the corresponding ratio of E to H.

The derived fracture toughness of the pillars with different out-of-plane orientations is in the range from 0.72 to 1.10 MPa·m$^{1/2}$ with an average value of 0.89 ± 0.13 MPa·m$^{1/2}$. The data used for the analysis according to equation (1), are summarized in detail in Table 2. As mentioned above, the grain size was 12.1 ± 5.9 μm. Therefore, the pillars of 10 μm nominal diameter were located inside single grains and the fracture toughness can be interpreted as intrinsic property of LATP material. The effect of the FIB preparation can be neglected, since a crack would propagate inside the pillar away from the surface affected by the Ga^+ ion beam [18, 46]. Similar as reported for Si pillars with different diameters, the fracture toughness can be expected to be insensitive to FIB effects, which is also in agreement with the observations on LLZO materials with different grain size [23].

Table 2. Summary of micro-pillar test results.

Pillar No.	Radius (μm)	Critical load (mN)	Ω	E/H	Fracture toughness (MPa·m$^{1/2}$)	Average fracture toughness (MPa·m$^{1/2}$)
1	5.4	31.5	62.2	22.2	0.98	
2	5.4	27.8	22.4	20.0	0.80	
3	5.2	22.4	70.2	21.7	0.72	
4	5.2	27.6	65.7	22.0	0.90	
5	5.2	34.0	69.6	21.7	1.10	
6	5.1	25.6	54.2	22.5	0.88	
7	5.1	35.9	11.9	18.3	1.02	0.89±0.13
9	5.5	35.0	65.7	22.0	1.03	
10	5.5	26.1	65.7	22.0	0.78	
11	5.5	24.2	51.7	22.5	0.75	
12	5.1	21.6	51.7	22.5	0.75	
13	5.5	28.0	48.5	22.5	0.85	
14	5.4	30.5	48.5	22.5	0.96	

In order to study the dependence of the intrinsic fracture toughness of LATP material on the grain orientation, the fracture toughness as a function of correlated angle is plotted in Fig. 5. The K_C is scattered showing no obvious dependency on the orientation

angle, especially compared to the E/H ratio in Fig. 4(b), which increased towards a plateau value with increasing angle from the basal plane. A number of factors can influence the results from micro-pillar splitting, including indenter positioning accuracy [46], the loading rate [46], indenter angle [47], testing temperature [48], pillar size [23, 46] and pre-existing defects [49]. In this work, the positioning effect can be neglected since the indenter tip was positioned based on a scan of the surface directly preceding the experiment, as well as the testing rate, indenter angle and testing temperature effects, which were fixed. Thus only the microstructure effect needs to be considered.

Pillars 11 and 12 located in the same grain exhibited almost the same fracture toughness value (see Table 2), whereas for pillars 9 and 10, and pillars 13 and 14, which were also located in single grains, clearly different fracture toughness values were determined. In addition to grain orientation effects, such differences could be related to the slightly varied pillar size and/or pre-existing pores (as seen in Fig. 6 (e)). Therefore, it can be concluded that the grain orientation has no significant influence on the intrinsic fracture toughness of LATP material. The fracture toughness results obtained in this study agree well with the data of Jackman et al. [12] determined from single-edge notched bend tests, and Athanasiou et al. [13] reporting 1.1 $MPa \cdot m^{1/2}$ with a rather high uncertainty. Therefore, the micro-pillar splitting test can be adopted for characterizing the fracture properties of porous LATP material.

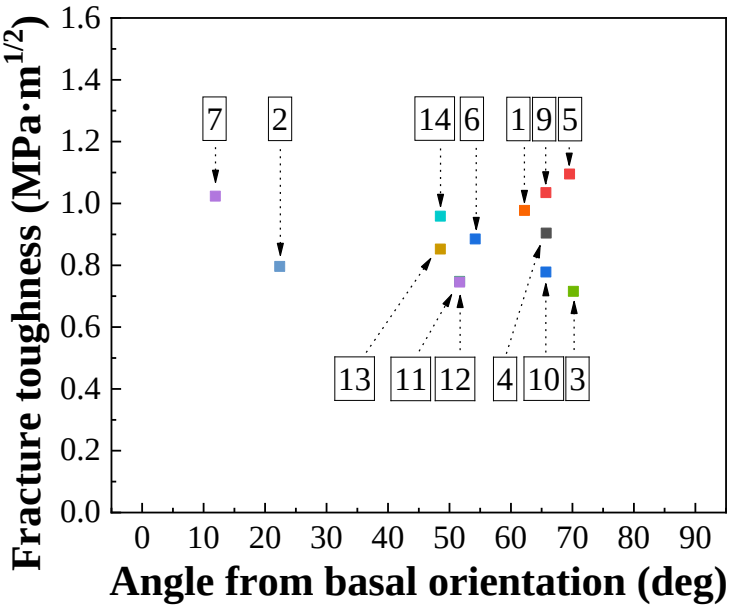

Figure 5. Fracture toughness of LATP material determined from micropillar splitting as a function of rotation angle from basal plane to prismatic plane. The results are summarized in Table 2.

The post-test images of the pillars are shown in Fig. 6. As can be seen in Fig. 3, some load-displacement curves of pillars show multiple pop-ins, while for some pillars the load never reached the set point of 50 mN, which was related to the crushing of those pillars as exemplified in Fig. 6(b). Since the micro-pillar splitting method only takes the critical load and energy, which initiated the crack, into account, the additional secondary cracks occurring at higher loads have no influence on the fracture toughness derivation.

To better understand the crack propagation after the pillar splitting, which is beneficial for comprehending the effect of the microstructural features, such as defects and the grain orientation, on the fracture toughness, FIB cross sections of the tested pillars were prepared as shown in Fig. 6 (c), (d) and (e) revealing different failure modes. Fig. 6 (c) shows the most frequently observed failure mode of axial splitting of the micro-pillar characteristic of brittle failure and often reported for pillar compression tests [50, 51]. The failure appears as a single crack or multiple vertical cracks formed near the pillar center, which can also be found in Fig. 6(d) and (e). The dashed lines in

Fig. 6(d) indicate the side splitting inside the pillar, with the cracks propagating towards the side-face of the pillar. This effect can be attributed to the transverse force component during loading/unloading generated on the contacting surface, leading to a tensile state of the deformed zone close to the indenter, which was constrained by the bottom part of the pillar. The side splitting might also be related to the activated glide planes of the rhombohedral structure, which needs to be further investigated in future studies [52].

As a porous ceramic material, the distribution of inhomogeneities or flaws cannot be neglected in the LATP material, even in the selected intact areas that appeared free from pores. The arrows in Fig. 6(e) mark the pre-existing weak interfaces, i.e., a pore and a grain boundary, which likely have led to premature failure thereby adding to the variation of the fracture toughness results.

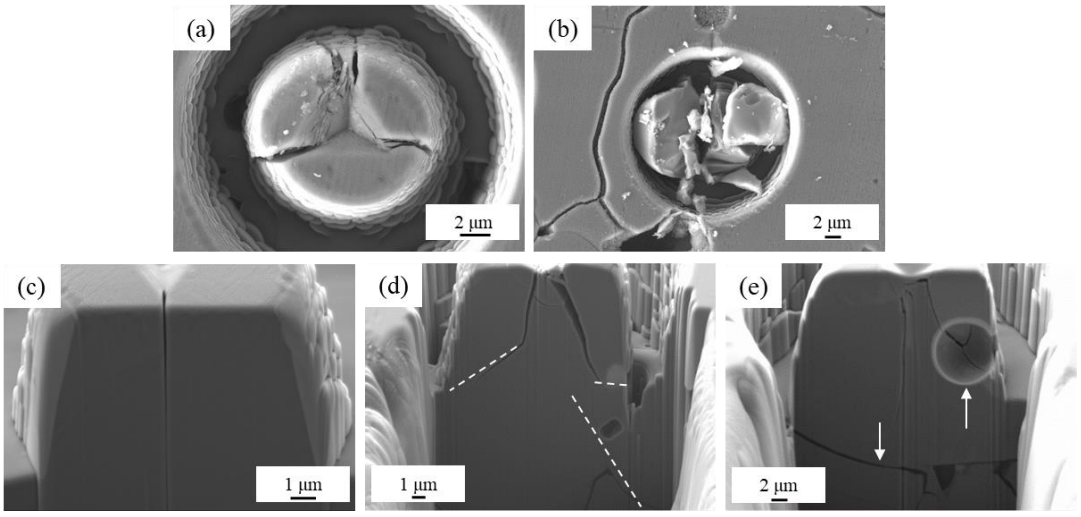

Figure 6. SEM micrographs of pillars after failure: typical top view of (a) a split pillar with the expected three-fold symmetry, and (b) a crushed pillar. FIB-prepared X-sections reveal (c) axial splitting, (d) side splitting, and (e) cracks located in the pillar interior likely caused by local material inhomogeneities.

Elastic modulus and hardness of the LATP sample obtained from indentation as a function of load are shown in Fig. 7. Both elastic modulus and hardness decrease with increasing indentation load and appear to gradually stabilize at higher loads. The

decrease of E and H with increasing indentation load, hence, increasing indentation depth and a larger deformed zone, is likely associated to an enhanced effect of porosity and weak grain boundaries [53-55]. The values of E and H determined at a load of 50 mN, i.e. 117.51 ± 10 GPa and 9.08 ± 1.31 GPa, respectively, were employed for VIF fracture toughness calculation of LATP.

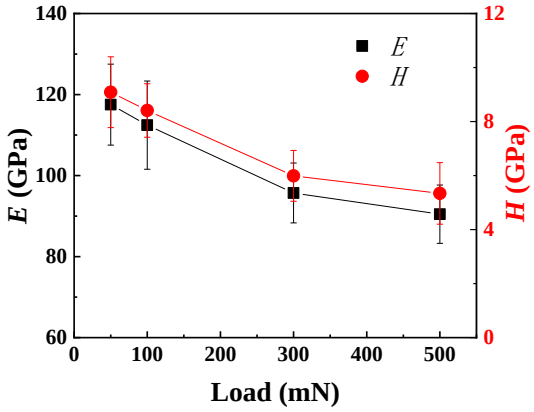

Figure 7. Elastic modulus (left axis, square symbols) and hardness (right axis, circle symbols) of LATP determined from indentation as function of load. The average of 20 experiments is shown with error bars representing one standard deviation.

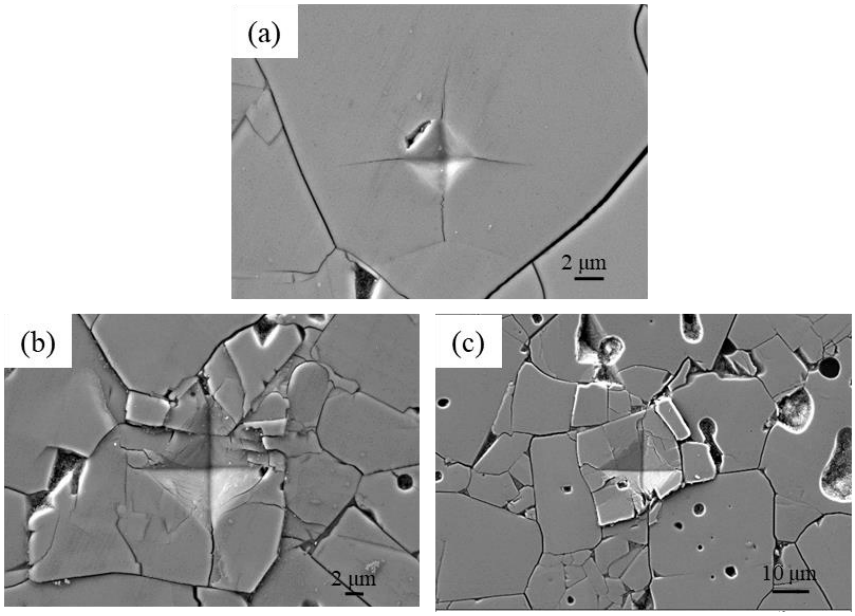

Figure 8. SEM images of Vickers imprints into LATP after loading to (a) 0.5 N, (b) 1 N and (c) 3 N. Note that the micrographs were obtained at different magnifications.

Conventional Vickers indentation fracture tests conducted at loads of 0.5 N, 1 N and 3 N to generate crack patterns on the LATP sample for the fracture toughness determination. Typical SEM images of imprints obtained at different loads are shown in Fig. 8. Even though the large apparently pore-free regions were chosen for the indentation, when observing the resultant impressions, cracks intersecting with the grain boundaries can be found for all loads. For the loads at 1 N and 3 N, the material was crushed and chipped off at the edge of the imprints, which can be ascribed to the pores and weak grain boundaries beneath the surface. Thus, for loads of 1 N and 3 N it was not possible to estimate the fracture toughness. Regarding the low load of 0.5 N, the determination of the crack length was also difficult as some cracks intersected with the grain boundaries. Hence, the fracture toughness results via VIF method represent the bulk material's behavior, and overall the VIF method can serve as a complementary method to the micro-pillar test. Adopting Niihara's Palmqvist equation [56], the fracture toughness was estimated as 0.79 ± 0.06 MPa·m$^{1/2}$, which is in agreement with our pillar splitting results as well as the literature [12, 13].

Although the results from the micro-pillar splitting and conventional VIF tests are in good agreement, these two testing methods and evaluation procedures are different, leading to the requirement of careful interpretation, which is discussed below. The application of the micro-pillar splitting test is quite straightforward using equation (1), of which the coefficient γ has been verified with a set of materials [18, 19]. The conventional VIF test is only an empirical method, the application of which to determine valid fracture toughness values is still under debate. Firstly, the VIF method correlates to an ill-determined crack capture condition [57]. In addition, the fracture mode needs to be determined depending on the l/a ratio and the appropriate equation needs to be selected [40]. For known E and H of a material, the micro-pillar splitting test requires only the critical load and pillar size, while the VIF method adopts a series of loads to generate regular cracks and requires precisely measured crack lengths. However, the micro-pillar splitting method also has some shortcomings. The fabrication

of micro pillars usually adopting FIB is more complex than just the surface polishing needed for VIF [22, 46, 58]. Additionally, a load- and depth-sensing indentation setup with sufficient load resolution is necessary, whereas for the VIF test loads in the Newton range are applied. Fracture toughness in general is measured as energy consumption of a crack propagating over the specimen at a certain length scale, depending on the material's structure and defects. Therefore, the sample for VIF testing should be prepared in larger size than that for micro-pillar splitting. Typically, the solid electrolytes applied in lithium batteries have a thickness of ~10 - ~100 microns [59, 60] and, thus, the micro-pillar splitting test is highly appropriate for studying the properties of LATP electrolyte at the application-relevant length scales.

Conclusion

Fracture toughness is a key property of the solid electrolyte expected to influence the all-solid-state lithium batteries' performance and long-term operation. In the present work, micro-pillar splitting tests were conducted to assess the fracture toughness of LATP material accounting for the anisotropic elastic modulus and hardness of the rhombohedral structure characterized in our previous work [20]. The fracture toughness of LATP obtained from micro-pillar splitting was 0.89 ± 0.13 $MPa \cdot m^{1/2}$, which is in good agreement with the macroscopic fracture toughness estimated from conventional VIF tests, i.e. 0.79 ± 0.06 $MPa \cdot m^{1/2}$, and with literature results [12, 13]. The conventional VIF test cannot be applied at loads greater than 0.5 N, since significant surface damage occurs at higher loads.

The results of this study indicate that the grain orientation has no pronounced influence on the intrinsic fracture toughness of LATP material, which might require further consideration in materials development and application. The micro-pillar splitting method is particularly useful to determine the fracture toughness on a local scale and of small-sized samples, such as solid electrolyte materials with thickness ~10 - ~100 microns, which are typical dimensions of the materials in application-relevant geometries. This work underscores the practical importance of the micro-pillar splitting

method for the characterization of anisotropic materials and adds to understanding of the mechanical characteristics of LATP material.

Acknowledgement

The authors would like to thank Dr. E. Wessel, Dr. D. Grüner and Mr. M. Ziegner for supporting the work with SEM, EBSD and XRD investigation. Gang Yan gratefully acknowledges the support from the China Scholarship Council (CSC) of China.

References

[1] M. Armand, J.-M. Tarascon, Building better batteries, Nature, 451 (2008) 652-657.

[2] B. Scrosati, J. Garche, Lithium batteries: Status, prospects and future, J Power Sources, 195 (2010) 2419-2430.

[3] J.O. Besenhard, Handbook of battery materials, John Wiley & Sons2008.

[4] J. Narváez-Semanate, A. Rodrigues, Microstructure and ionic conductivity of $Li_{1+x}Al_xTi_{2-x}(PO_4)_3$ NASICON glass-ceramics, Solid State Ionics, 181 (2010) 1197-1204.

[5] W. Zhou, S. Wang, Y. Li, S. Xin, A. Manthiram, J.B. Goodenough, Plating a dendrite-free lithium anode with a polymer/ceramic/polymer sandwich electrolyte, J Am Chem Soc, 138 (2016) 9385-9388.

[6] Y. Shao, F. Ding, J. Xiao, J. Zhang, W. Xu, S. Park, J.G. Zhang, Y. Wang, J. Liu, Making Li‐air batteries rechargeable: Material challenges, Adv Funct Mater, 23 (2013) 987-1004.

[7] K. Kerman, A. Luntz, V. Viswanathan, Y.-M. Chiang, Z. Chen, practical challenges hindering the development of solid state Li ion batteries, J Electrochem Soc, 164 (2017) A1731-A1744.

[8] P. Verma, P. Maire, P. Novák, A review of the features and analyses of the solid electrolyte interphase in Li-ion batteries, Electrochim Acta, 55 (2010) 6332-6341.

[9] J. Xu, B.H. Liu, D.Y. Hu, State of Charge Dependent Mechanical Integrity Behavior of 18650 Lithium-ion Batteries, Sci Rep-Uk, 6 (2016).

[10] P. Balakrishnan, R. Ramesh, T.P. Kumar, Safety mechanisms in lithium-ion batteries, J Power Sources, 155 (2006) 401-414.

[11] X. Hu, X. Cheng, S. Qin, G. Yan, J. Malzbender, W. Qiang, B. Huang, Mechanical and electrochemical properties of cubic and tetragonal $Li_xLa_{0.557}TiO_3$ perovskite oxide electrolytes, Ceram Int, 44 (2018) 1902-1908.

[12] S.D. Jackman, R.A. Cutler, Effect of microcracking on ionic conductivity in LATP, J Power Sources, 218 (2012) 65-72.

[13] C.E. Athanasiou, M.Y. Jin, C. Ramirez, N.P. Padture, B.W.J.M. Sheldon, High-Toughness Inorganic Solid Electrolytes via the Use of Reduced Graphene Oxide, (2020).

[14] E. Dashjav, M. Gellert, G. Yan, D. Grüner, N. Kaiser, S. Spannenberger, I. Kraleva, R. Bermejo, M.-T. Gerhards, Q.J.J.o.t.E.C.S. Ma, Microstructure, ionic conductivity and mechanical properties of tape-cast $Li_{1.5}Al_{0.5}Ti_{1.5}P_3O_{12}$ electrolyte sheets, 40 (2020) 1975-1982.

[15] X.-K. Zhu, J.A. Joyce, Review of fracture toughness (G, K, J, CTOD, CTOA) testing and standardization, Engineering Fracture Mechanics, 85 (2012) 1-46.

[16] J.P. Best, J. Zechner, J.M. Wheeler, R. Schoeppner, M. Morstein, J. Michler, Small-scale fracture toughness of ceramic thin films: the effects of specimen geometry, ion beam notching and high temperature on chromium nitride toughness evaluation, Philos Mag, 96 (2016) 3552-3569.

[17] G.D. Quinn, Fracture toughness of ceramics by the Vickers indentation crack length method: a critical review, Ceramic engineering and science proceedings, American Ceramic Society, 2007, pp. 45.

[18] M. Sebastiani, K. Johanns, E.G. Herbert, G.M. Pharr, Measurement of fracture toughness by nanoindentation methods: Recent advances and future challenges, Current Opinion in Solid State and Materials Science, 19 (2015) 324-333.
[19] M. Sebastiani, K.E. Johanns, E.G. Herbert, F. Carassiti, G.M. Pharr, A novel pillar indentation splitting test for measuring fracture toughness of thin ceramic coatings, Philos Mag, 95 (2015) 1928-1944.
[20] G. Yan, S. Yu, W. Yang, X. Li, H. Tempel, H. Kungl, R.-A. Eichel, M. Krüger, J.J.J.o.P.S. Malzbender, Anisotropy of the mechanical properties of $Li_{1.3}Al_{0.3}Ti_{1.7}(PO_4)_3$ solid electrolyte material, 437 (2019) 226940.
[21] Z. Deng, Z. Wang, I.-H. Chu, J. Luo, S.P. Ong, Elastic properties of alkali superionic conductor electrolytes from first principles calculations, J Electrochem Soc, 163 (2016) A67-A74.
[22] A.-N. Wang, J.F. Nonemacher, G. Yan, M. Finsterbusch, J. Malzbender, M. Krüger, Mechanical properties of the solid electrolyte Al-substituted $Li_7La_3Zr_2O_{12}$ (LLZO) by utilizing micro-pillar indentation splitting test, J Eur Ceram Soc, (2018).
[23] J.F. Nonemacher, Y. Arinicheva, G. Yan, M. Finsterbusch, M. Krüger, J. Malzbender, Fracture toughness of single grains and polycrystalline Li7La3Zr2012 electrolyte material based on a pillar splitting method, J Eur Ceram Soc, (2020).
[24] M.Z. Mughal, R. Moscatelli, H.-Y. Amanieu, M.J.S.M. Sebastiani, Effect of lithiation on micro-scale fracture toughness of $LixMn_2O_4$ cathode, 116 (2016) 62-66.
[25] S. Yu, A. Mertens, X. Gao, D.C. Gunduz, R. Schierholz, S. Benning, F. Hausen, J. Mertens, H. Kungl, H. Tempel, Influence of microstructure and AlPO4 secondary-phase on the ionic conductivity of $Li_{1.3}Al_{0.3}Ti_{1.7}(PO_4)_3$ solid-state electrolyte, Functional Materials Letters, 9 (2016) 1650066.
[26] G. Yan, S. Yu, J.F. Nonemacher, H. Tempel, H. Kungl, J. Malzbender, R.-A. Eichel, M. Krüger, Influence of sintering temperature on conductivity and mechanical behavior of the solid electrolyte LATP, Ceram Int, 45 (2019) 14697-14703.
[27] H. Aono, E. Sugimoto, Y. Sadaaka, N. Imanaka, G.J.J.o.t.E.S. Adachi, Ionic conductivity of the lithium titanium phosphate $(Li_{1+x}M_xTi_{2-x}(PO_4)_3$, M= Al, Sc, Y, and La) systems, 136 (1989) 590.
[28] X. Yu, J. Bates, G. Jellison, F. Hart, A stable thin‐film lithium electrolyte: lithium phosphorus oxynitride, J Electrochem Soc, 144 (1997) 524-532.
[29] R. Kanno, M. Maruyama, Lithium ionic conductor thio-LISICON - The Li_2S-GeS_2-P_2S_5 system, J Electrochem Soc, 148 (2001) A742-A746.
[30] R. Kanno, T. Hata, Y. Kawamoto, M. Irie, Synthesis of a new lithium ionic conductor, thio-LISICON-lithium germanium sulfide system, Solid State Ionics, 130 (2000) 97-104.
[31] Z.Q. Liu, F.Q. Huang, J.H. Yang, B.F. Wang, J.K. Sun, New lithium ion conductor, thio-LISICON lithium zirconium sulfide system, Solid State Ionics, 179 (2008) 1714-1716.
[32] J. Guo, S. Amira, P. Gougeon, X.-G.J.M.c. Chen, Effect of the surface preparation techniques on the EBSD analysis of a friction stir welded AA1100-B4C metal matrix composite, 62 (2011) 865-877.
[33] F. Bachmann, R. Hielscher, H. Schaeben, Texture analysis with MTEX‐free and

open source software toolbox, Solid State Phenomena, Trans Tech Publ, 2010, pp. 63-68.
[34] J. Clayton, Modeling finite deformations in trigonal ceramic crystals with lattice defects, International Journal of Plasticity, 26 (2010) 1357-1386.
[35] J. Ast, M. Ghidelli, K. Durst, M. Göken, M. Sebastiani, A.J.M. Korsunsky, Design, A review of experimental approaches to fracture toughness evaluation at the micro-scale, 173 (2019) 107762.
[36] A.J. Lunt, G. Mohanty, T.K. Neo, J. Michler, A.M. Korsunsky, Microscale resolution fracture toughness profiling at the zirconia-porcelain interface in dental prostheses, Micro+ Nano Materials, Devices, and Systems, International Society for Optics and Photonics, 2015, pp. 96685S.
[37] M. Ghidelli, M. Sebastiani, K.E. Johanns, G.M.J.J.o.t.A.C.S. Pharr, Effects of indenter angle on micro‐scale fracture toughness measurement by pillar splitting, 100 (2017) 5731-5738.
[38] W.C. Oliver, G.M. Pharr, An Improved Technique for Determining Hardness and Elastic-Modulus Using Load and Displacement Sensing Indentation Experiments, J Mater Res, 7 (1992) 1564-1583.
[39] C.B. Carter, M.G. Norton, Ceramic materials: science and engineering, Springer Science & Business Media2007.
[40] F. Sergejev, M. Antonov, Comparative study on indentation fracture toughness measurements of cemented carbides, Proc. Estonian Acad. Sci. Eng, 12 (2006) 388-398.
[41] J.-F. Yang, G.-J. Zhang, T. Ohji, Porosity and microstructure control of porous ceramics by partial hot pressing, J Mater Res, 16 (2001) 1916-1918.
[42] R. Kali, A. Mukhopadhyay, Spark plasma sintered/synthesized dense and nanostructured materials for solid-state Li-ion batteries: Overview and perspective, J Power Sources, 247 (2014) 920-931.
[43] W. Zhou, J. Malzbender, F. Zeng, W. Deibert, O. Guillon, R. Schwaiger, W.A. Meulenberg, Mechanical properties of $BaCe_{0.65}Zr_{0.2}Y_{0.15}O_{3-\delta}$ proton-conducting material determined using different nanoindentation methods, J Eur Ceram Soc, 40 (2020) 5653-5661.
[44] T. Csanádi, D. Németh, J. Dusza, Z. Lenčéš, P. Šajgalík, Nanoindentation induced deformation anisotropy in β-Si_3N_4 ceramic crystals, J Eur Ceram Soc, 36 (2016) 3059-3066.
[45] T. Csanádi, A. Kovalčíková, J. Dusza, W.G. Fahrenholtz, G.E. Hilmas, Slip activation controlled nanohardness anisotropy of ZrB_2 ceramic grains, Acta Mater, 140 (2017) 452-464.
[46] C.M. Lauener, L. Petho, M. Chen, Y. Xiao, J. Michler, J.M.J.M. Wheeler, Design, Fracture of silicon: influence of rate, positioning accuracy, FIB machining, and elevated temperatures on toughness measured by pillar indentation splitting, 142 (2018) 340-349.
[47] M. Ghidelli, M. Sebastiani, K.E. Johanns, G.M. Pharr, Effects of indenter angle on micro-scale fracture toughness measurement by pillar splitting, 100 (2017) 5731-5738.
[48] J.P. Best, J. Wehrs, M. Polyakov, M. Morstein, J.J.S.M. Michler, High temperature

fracture toughness of ceramic coatings evaluated using micro-pillar splitting, 162 (2019) 190-194.
[49] J. Schwiedrzik, R. Raghavan, A. Bürki, V. LeNader, U. Wolfram, J. Michler, P.J.N.m. Zysset, In situ micropillar compression reveals superior strength and ductility but an absence of damage in lamellar bone, 13 (2014) 740-747.
[50] F. Östlund, K. Rzepiejewska‐Malyska, K. Leifer, L.M. Hale, Y. Tang, R. Ballarini, W.W. Gerberich, J.J.A.F.M. Michler, Brittle‐to‐ductile transition in uniaxial compression of silicon pillars at room temperature, 19 (2009) 2439-2444.
[51] F. Östlund, P.R. Howie, R. Ghisleni, S. Korte, K. Leifer, W.J. Clegg, J. Michler, Ductile‐brittle transition in micropillar compression of GaAs at room temperature, Philos Mag, 91 (2011) 1190-1199.
[52] C. Zambaldi, Y. Yang, T.R. Bieler, D.J.J.o.M.R. Raabe, Orientation informed nanoindentation of [alpha]-titanium: Indentation pileup in hexagonal metals deforming by prismatic slip, 27 (2012) 356.
[53] A. Krell, S.J.M.S. Schädlich, E. A, Nanoindentation hardness of submicrometer alumina ceramics, 307 (2001) 172-181.
[54] Z. Peng, J. Gong, H.J.J.o.t.E.C.S. Miao, On the description of indentation size effect in hardness testing for ceramics: Analysis of the nanoindentation data, 24 (2004) 2193-2201.
[55] I. Manika, J.J.A.m. Maniks, Size effects in micro-and nanoscale indentation, 54 (2006) 2049-2056.
[56] K. Niihara, R. Morena, D. Hasselman, Evaluation of KIc of brittle solids by the indentation method with low crack-to-indent ratios, Journal of Materials Science Letters, 1 (1982) 13-16.
[57] G.D. Quinn, R.C. Bradt, On the Vickers indentation fracture toughness test, J Am Ceram Soc, 90 (2007) 673-680.
[58] S. Bruns, L. Petho, C. Minnert, J. Michler, K.J.M. Durst, Design, Fracture toughness determination of fused silica by cube corner indentation cracking and pillar splitting, 186 (2020) 108311.
[59] X.-B. Cheng, R. Zhang, C.-Z. Zhao, Q. Zhang, Toward safe lithium metal anode in rechargeable batteries: a review, Chemical reviews, 117 (2017) 10403-10473.
[60] Y. Wang, B. Liu, Q. Li, S. Cartmell, S. Ferrara, Z.D. Deng, J. Xiao, Lithium and lithium ion batteries for applications in microelectronic devices: A review, J Power Sources, 286 (2015) 330-345.